ISSN 1024-8560, Atmospheric and Oceanic Optics, 2017, Vol. 30, No. 1, pp. 103–110. © Pleiades Publishing, Ltd., 2017.
Original Russian Text © T.B. Zhuravleva, I.M. Nasrtdinov, T.V. Russkova, 2017, published in Optika Atmosfery i Okeana.

OPTICAL MODELS AND DATABASES

Influence of 3D Cloud Effects on Spatial-Angular Characteristics of the Reflected Solar Radiation Field

T. B. Zhuravleva*, I. M. Nasrtdinov, and T. V. Russkova*****

V.E. Zuev Institute of Atmospheric Optics, Siberian Branch, Russian Academy of Sciences, Tomsk, 634055 Russia

**e-mail: ztb@iao.ru*

***e-mail: wizard@iao.ru*

****e-mail: btv@iao.ru*

Received April 4, 2016

Abstract—Spatial-angular characteristics of reflected solar radiation in broken clouds are simulated in the spherical model of the atmosphere using statistical algorithms developed in the Institute of Atmospheric Optics, Siberian Branch, Russian Academy of Sciences. The patterns of formation of radiance fields of scattered radiation, caused by the finite cloud extents, mutual cloud shading, and radiation re-reflection by neighboring cloud elements are considered by the example of individual cloud realizations. It is shown that, for small and moderate cloud fractions, the specific features of the radiance field of reflected solar radiation are mainly determined by cloud localization relative to the viewing direction and direction "toward the Sun".

Keywords: solar radiation, Monte Carlo method, isolated cloud, broken clouds, 3D cloud effects

DOI: 10.1134/S102485601701016X

INTRODUCTION

Operational algorithms, designed to retrieve the optical and microphysical characteristics of clouds and aerosol from data of satellite measurements of solar radiation, are based on solution of the radiative transfer equation in the horizontally homogeneous model of the Earth's atmosphere. This approximation assumes that the radiative properties of an individual pixel depend on surrounding elements. At the same time, many studies have shown (see, e.g., [1–4]) that the intrinsic inhomogeneous cloud field structure has a significant effect on retrieved cloud properties. No less important task is to account for the cloud effect on retrieved aerosol characteristics (aerosol optical depth (AOD), the Ångström exponent, fine fraction) in cloud gaps near cloud pixels [5–9]. Based on analysis of ground-based and satellite radiation measurements, a number of authors [6, 8–10] note an increase in sky radiance in these regions of space.

Aside from the effect of instrumental features of radiometers, the reasons for radiance enhancements near clouds are conventionally divided into two groups: cloud-aerosol interaction (increases in sizes and concentration of aerosol particles, the presence of cloud particles leaving out the cloud "borders", etc. [8, 11, 12]) and 3D cloud effects [5, 9, 13]. To date, there are no estimates of the relative contribution of each of these components to changes in the spectral-angular characteristics of reflected solar radiation. At the same time, studies of satellite data confirm that certain regularities in the behavior of sky radiance (brightness of cloud-free gaps increases stronger on sunlit side and near optically dense clouds, as well as at shorter wavelengths) may be just due to 3D cloud effects [7, 9, 13, 14].

Theoretical estimates of sky radiance variations near clouds are scarce and obtained using quite simple cloud models: isolated clouds shaped as a rectangular parallelepiped [15], an infinitely long cuboidal bar [16], and a horizontal semi-infinite cloud [17, 18]. In the present work, we consider the results of numerical simulation of angular characteristics of reflected solar radiation in the presence of an isolated cloud (inverted truncated paraboloid) and mesoscale cloud fields (modeled on Poisson point fluxes in space) in the visible spectral range. The purpose of the paper is (1) to identify the main factors, determining specific features of formation of radiance fields of broken clouds; and (2) to compare the sky radiances in the absence and in the presence of clouds for different geometries of experiment and configurations of clouds in space.

1. MODEL AND METHOD OF SOLUTION

The angular characteristics of the radiation field were simulated in the spherical model of the atmosphere, specified in a global Cartesian coordinate system *OXYZ* (GCS), the center of which coincides with the Earth's center (point *O*), while the *OZ* axis is determined by the position of the detector (point *A*) at the top of the atmosphere (TOA). The results of the

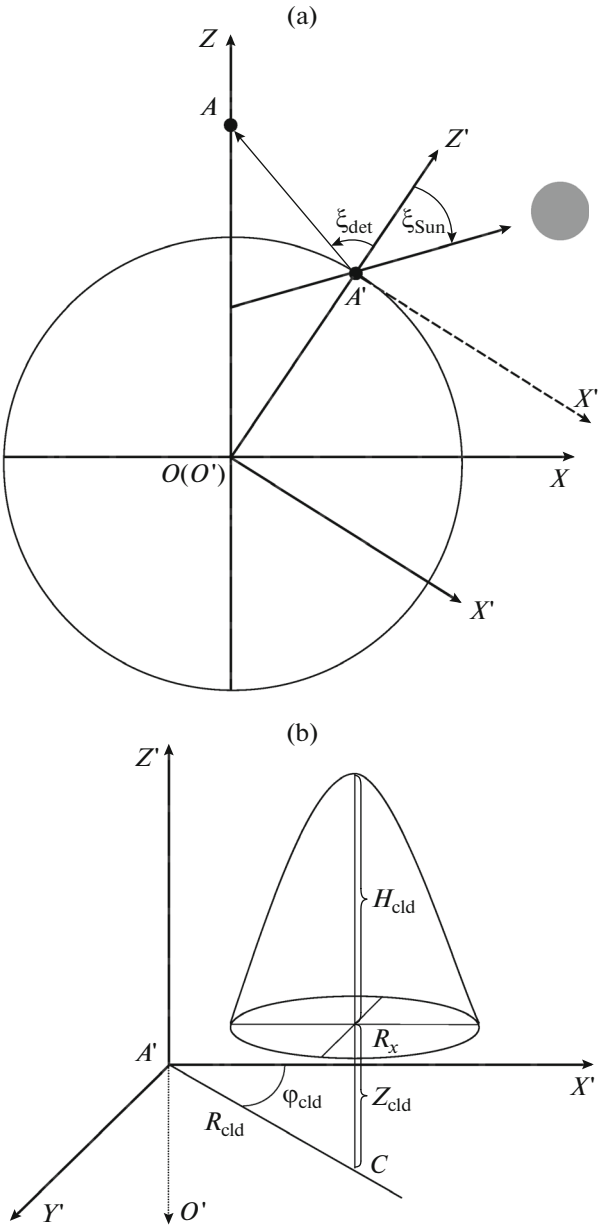

Fig. 1. (a) Local and global coordinate systems for observations from space and (b) geometry of cloud position in local coordinate system.

numerical simulation are represented in the local coordinate system $O'X'Y'Z'$ (LCS), defined by its center $O' = O$ and the $O'Z'$ axis, passing through the observation point A' on the Earth's surface (Fig. 1a). Directions "toward detector" and "toward the Sun" in LCS are defined by zenith and azimuth angles: $\omega_{det} = (\xi_{det}, \varphi_{det})$ and $\omega_{Sun} = (\xi_{Sun}, \varphi_{Sun})$. Zenith angles are measured from the positive direction of the $O'Z'$ axis. The positive direction of $O'X'$ axis is chosen such that $\varphi_{det} = 180°$. The azimuth angle $\varphi_{Sun} = 0$ corresponds to the configuration when in the $O'X'Z'$ plane the detector and Sun are on opposite sides of $O'Z'$ axis; while at $\varphi_{Sun} = 180°$, the Sun is "behind" the observer. Conversion from LCS to GCS is performed by means of elementary formulas.

The number of cloud centers N in a realization with the area S is simulated according to the Poisson law and is determined from the formula [19]:

$$N = \min\{i : \prod_{k=0}^{i} \alpha_k < e^{-\eta S}\},$$
$$\eta = -\ln(1 - 0.1|CF)/S_{sec}, \quad (1)$$

where CF is the cloud fraction (varies from 0 to 10); and S_{sec} is the cloud base area. Uniformly distributed points (cloud centers) on a curvilinear surface are simulated in accordance with approach [20]. Clouds are approximated by inverted truncated paraboloids of rotation with base semiaxes $R_x = R_y$ and geometrical thickness H_{cld}. Since the cloud amount is determined at random and cloud bases may intersect, after simulation of a realization we calculated the actual cloud fraction CF_1 which could differ from the specified CF in formula (1). In this work, for simulating the radiation characteristics we selected such cloud field realizations, in which the difference $|CF - CF_1|$ did not exceed 0.1. The cloud center was determined in the shifted local coordinate system ($O' \to A'$) $X'Y'Z'$ by distance between the observation point A' and projection of the paraboloid center onto the Earth (C), azimuth angle φ_{cld} between the rays $A'X'$ and $A'C$, and height of the cloud base center above the Earth's surface Z_{cld} (Fig. 1b).

The scattered solar radiation in the deterministic horizontally and vertically inhomogeneous atmosphere was simulated using our statistical algorithms based on the method of adjoint walks [21, 22]. In accordance with efficiency estimates, the radiation characteristics were calculated using different modifications of this method, differing in the way of simulating the free path length: canonical procedures of analogue simulation in slightly overcast situations and method of maximal cross section for large cloud fractions [23]. The molecular absorption was accounted for by assuming that the transmission function of atmospheric gases is represented as short exponential series (k-distribution method).

Parallel flux of monochromatic solar radiation with the power πS_λ is incident at the top of the atmosphere (TOA = 100 km). The incident radiation is reflected from the underlying surface according to the Lambert law. The optical characteristics of the vertically inhomogeneous aerosol-molecular atmosphere (extinction coefficients, scattering phase functions and single scattering albedo of aerosol particles, molecular scattering and absorption coefficients) are specified in the form of piecewise constant functions according to the models [24, 25]. In spatial regions occupied by cloud elements, the optical characteristics are determined according to standard mixing rules in the medium consisting of different components (clouds, aerosol, air molecules).

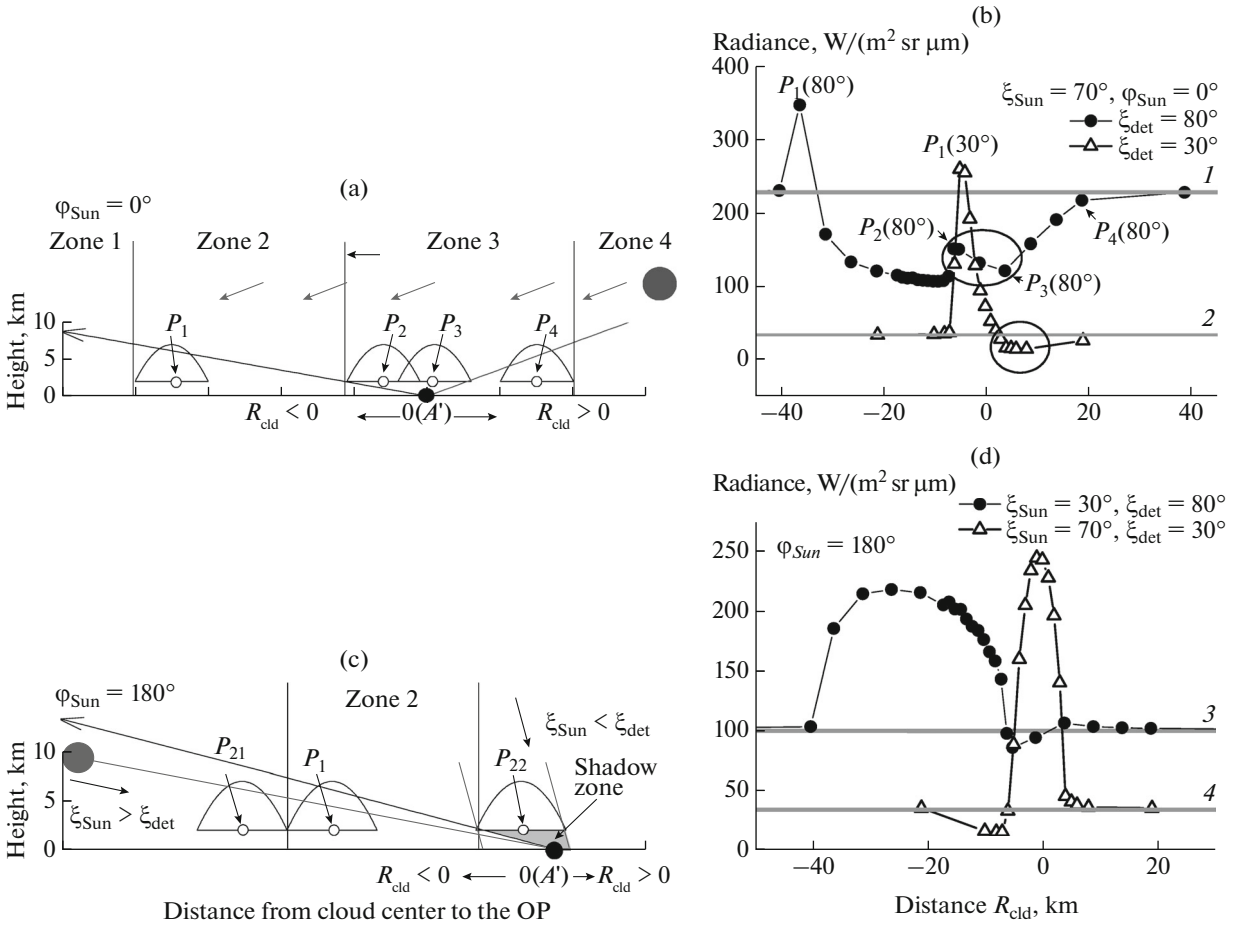

Fig. 2. (a, c) Schematic illustration of sensing of isolated cloud for different illumination conditions; (b, d) the dependence of sky radiance in the presence of cloud for different observation conditions compared to clear-sky conditions (straight lines *1–4*).

In this work, we present the results of simulation of sky radiance in the visible wavelength range (0.55–0.555 μm). Cloud parameters are fixed: $R_x = H_{cld} =$ 5 km; $Z_{cld} = 2$ km; extinction coefficient $\sigma_{cld} = 5$ km^{-1}; surface albedo was equal to 0.106 (grass, [26]), aerosol optical depth was assumed to be AOD (0.55 μm) = 0.15.

2. ISOLATED CLOUD

Analysis of numerical simulation results showed that sky radiance in the presence of isolated cloud depends on a set of factors that can be conventionally divided into geometrical (viewing directions and illumination conditions, vertical and horizontal cloud sizes, cloud position in space) and optical factors (optical depth, scattering phase function, and single scattering albedo of cloud particles). Below, we discuss the effects caused by the effect of geometrical factors.

The spatial and angular characteristics of the sky radiance field were simulated under the assumption that the *O'X'Y* plane, to which the line of sight (LS) belongs, divides the cloud into two equal parts. Negative R_{cld} values correspond to a cloud position "to the left" of the observation point (OP) *A'* ("closer" to satellite detector, $\varphi_{cld} = 180°$); when $R_{cld} > 0$ the cloud is "to the right" of the OP ($\varphi_{cld} = 0$). We consider diverse geometries of experiment, differing in the viewing angles of detector and illumination conditions ($\varphi_{Sun} = 0$ and $\varphi_{Sun} = 180°$).

The case when $\varphi_{Sun} = 0$ (detector and Sun "are one in front of another", Fig. 2a).

If the cloud is at quite a large distance from the OP, it has almost no effect on sky radiance (zone 1 and zone 4, Fig. 2a). For fixed cloud parameters and illumination conditions, the boundaries of these zones depend on detector zenith angle. For instance, at $\xi_{det} = 80°$, the sky radiances in the presence of cloud (I_{cld}) and in its absence (I_{clr}) are almost the same, if the distance between the projection of the cloud center and OP exceeds approximately 40 km; for $\xi_{det} = 30°$, the radius of the cloud impact zone reduces to 20 km (Fig. 2b). As the cloud approaches LS, its effect will be manifested as cloud-reflected radiation. However, additional illumination of the LS is much larger if the detector is directed toward sunlit cloud side ($\varphi_{Sun} =$ 180°).

In zone 2, the cloud is on the LS (point P_1) and the sky radiance I_{cld} is determined by two opposite factors. On one hand, as cloud approaches the point A', there are more, as compared to the clear-sky atmosphere, scatterers on the LS, favoring an increase in radiance. Considering that the cloud is approximated by a truncated paraboloid, as the cloud moves toward the OP, the number of scatterers first grows, and then decreases. On the other hand, of importance is the photon optical pathlength in the cloud (in terms of the single scattering theory, it is determined by the sum of photon optical paths (1) from the point of photon entry into the cloud to the LS, and (2) from the scattering point on the LS to exit from the cloud). The greater the photon optical pathlength in the cloud, the smaller the sky radiance is.

After a cloud "enters" the LS, such factors as the increase in the number of scatterers and relatively small photon optical pathlength within the cloud element start to dominate. As a consequence, I_{cld} rapidly increases as compared to clear-sky radiance I_{clr} (points $P_1(30°)$ and $P_1(80°)$ in Fig. 2b). As the cloud center approaches the OP, the effect of the second factor intensifies, causing decay of the sky radiance and its decrease as compared to I_{clr}.

The boundary between zones 2 and 3 is the point P_2, when the LS does not transect the cloud and no extra attenuation of radiation along this direction within the cloud occurs (Fig. 2a). When the cloud has a fixed size, the radiance is determined by the cloud position relative to the OP and illumination conditions: (1) for different combinations of ξ_{det} and ξ_{Sun}, the lower part of the LS, adjoining the surface, can be shaded or exposed to direct solar rays; (2) the length and position of shaded part of the LS can vary. Since the lower part of the atmosphere is the most optically dense, these factors determine the specific features of variations in sky radiance when the cloud passes zone 3. We will consider the results of simulation for solar zenith angle $\xi_{Sun} = 70°$ (Fig. 2b).

If $\xi_{det} = 30°$, then the position of the cloud center at the time when it "leaves" LS will be approximately 3.85 km; the OP and lower part of the atmosphere are shaded by the cloud. As the cloud moves farther away from the point A', radiances smaller than I_{clr} are observed, primarily because of shading of the LS segment adjoining the surface. At distance $R_{cld} > 20$ km, OP and LS become totally exposed to direct solar rays and the cloud effect on sky radiance vanishes ($I_{clr} \approx I_{cld}$).

For large detector zenith angles ($\xi_{det} = 80°$), the variations in sky radiance as a function of R_{cld} become more complex in character. When cloud "leaves" the LS ($R_{cld} \approx -6.35$ km), the surface-adjoining part of the LS, which is brightest owing to a large number of scatterers, is sunlit. Moreover, the observation point A' is exposed to direct solar radiation, causing an additional contribution of surface-reflected incident radiation to I_{cld}. The joint effect of these factors leads to an increase in sky radiance and the appearance of a local maximum (point $P_2(80°)$, Fig. 2b). As the cloud center moves further, the length of shaded part of the LS remains the same, but its position is displaced closer to the surface; thus, cloud shades the lower, brightest, part of the atmosphere (at the point P_3, the surface-adjoining LS segment is shaded maximally; the corresponding position of the cloud center $R_{cld} \approx 0.5$ km). A consequence of this is that I_{cld} decreases and the second local minimum is observed at the point P_3 ($P_3(80°)$, Fig. 2b). As the cloud moves further, the shaded LS segment decreases (point P_4), and the radiance I_{cld} gradually increases and approaches asymptotically the clear-sky radiance.

The case when $\varphi_{Sun} = 180°$ (Sun is "behind" the observer, Fig. 2c).

As in the case when $\varphi_{Sun} = 0$, there are regions of space within which the cloud has no disturbing effect on sky radiance as compared to the clear-sky atmosphere (Fig. 2c). However, in contrast to the geometry of the experiment, considered above, the sunlit part of the cloud strongly reflects (photon penetration depth into the cloud is on the average small). In addition, radiation produced inside a cloud element also contributes to the recorded signal.

When in zone 2, the cloud is intersected by the LS (point P_1 in Fig. 2c). The produced I_{cld} enhancement over I_{clr} is observed when the position of the cloud center is in the intervals from approximately −6.15 to 3.85 km when $\xi_{det} = 30°$ and from −40 to −6.35 km when $\xi_{det} = 80°$. In these regions, the sky radiance is determined by the above-mentioned factors, i.e., appearance of additional scatterers and change in photon optical path length in the cloud. The competing character of these factors explains the nonmonotonic behavior of the sky radiance as a function of R_{cld} (Fig. 2d).

Variations in sky radiance outside zone 2 are determined by the position of the cloud shadow on the LS. We will consider two situations: $\xi_{Sun} < \xi_{det}$ and $\xi_{Sun} > \xi_{det}$ (Fig. 2c). For conditions when $\xi_{Sun} = 30° < \xi_{det} = 80°$, the LS is shaded by the cloud when the cloud "leaves" the LS at the point P_{22} (the shadow zone is highlighted in Fig. 2c). For the geometry of experiment with $\xi_{Sun} = 70° > \xi_{det} = 30°$, the shadow region is formed before the cloud "enters" into zone 2 (point P_{21} in Fig. 2c). In both cases, LS shading causes the sky radiance to decrease versus the clear-sky case: $I_{cld} < I_{clr}$. Additional illumination is quite weakly exhibited for these calculation parameters.

3. MESOSCALE BROKEN CLOUD FIELD

In section 2, we studied the changes in the clear-sky radiance with the appearance of an isolated cloud

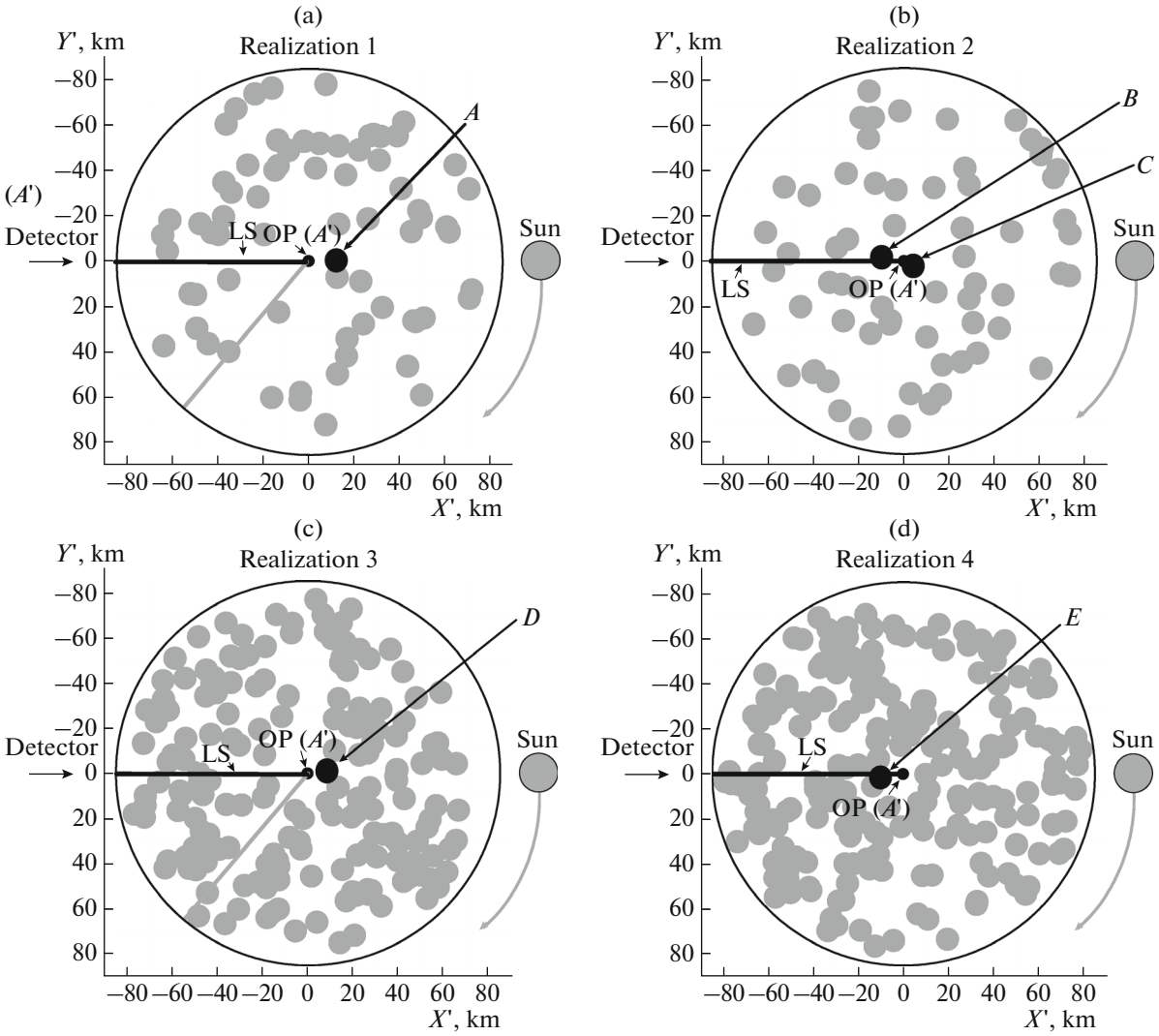

Fig. 3. Cloud realizations for two cloud fractions *CF*: (a) realization 1, (b) realization 2 ($CF = 2$); (c) realization 3, and (d) realization 4 ($CF = 5$). In realizations 1 and 3, the LS does not transect the cloud; and in realizations 2 and 4, the LS transects the cloud.

in the sky. In the transition to cloud fields, the behavior of sky radiance I_{cld} for fixed ξ_{det}, illumination conditions, and optical-geometrical cloud characteristics is determined by the configuration of the cloud field. The I_{cld} variations are determined by the cloud presence/absence on the line of sight, LS shading by clouds/nonobscuration of direction "toward the Sun", as well as possible LS illumination by nearby clouds. This is complemented by the effects of mutual cloud shading and radiation interaction, when part of the radiation, leaving through a cloud lateral surface, can be multiply scattered by surrounding clouds.

The joint effect of these factors is discussed below by the example of individual cloud realizations and a fixed detector angle $\xi_{det} = 60°$. The cloud field area was assumed to be 22 500 km^2, the radius of the corresponding "circle" on the surface of the sphere was ~ 84.5 km; the cloud field center was above the observation point (LCS center). We will analyze the situations corresponding to the conditions when $0 \le \varphi_{Sun} \le 180°$.

Figure 3 presents the projections of four different cloud field realizations onto the $X'O'Y'$ plane at cloud fractions $CF = 2$ and $CF = 5$. Realizations 1 and 3 are characterized by the absence of clouds on the LS (Figs. 3a and 3c); while in realizations 2 and 4 the LS transects the cloud (Figs. 3b and 3d).

We will consider how sky radiance I_{cld} changes as the illumination conditions vary in realizations 1 and 3.

Assume that $\varphi_{Sun} = 0$ (Fig. 4a). When the LS is not obscured, the sky radiance can be affected by (1) radiation reflected from LS-adjacent clouds and (2) shading of LS and observation point A' by clouds lying in the direction "toward the Sun".

Cloud A ($R_{cld} \approx 12$ km, Fig. 3a) is located near the observation point in realization 1. For $\xi_{Sun} < 55°$ and

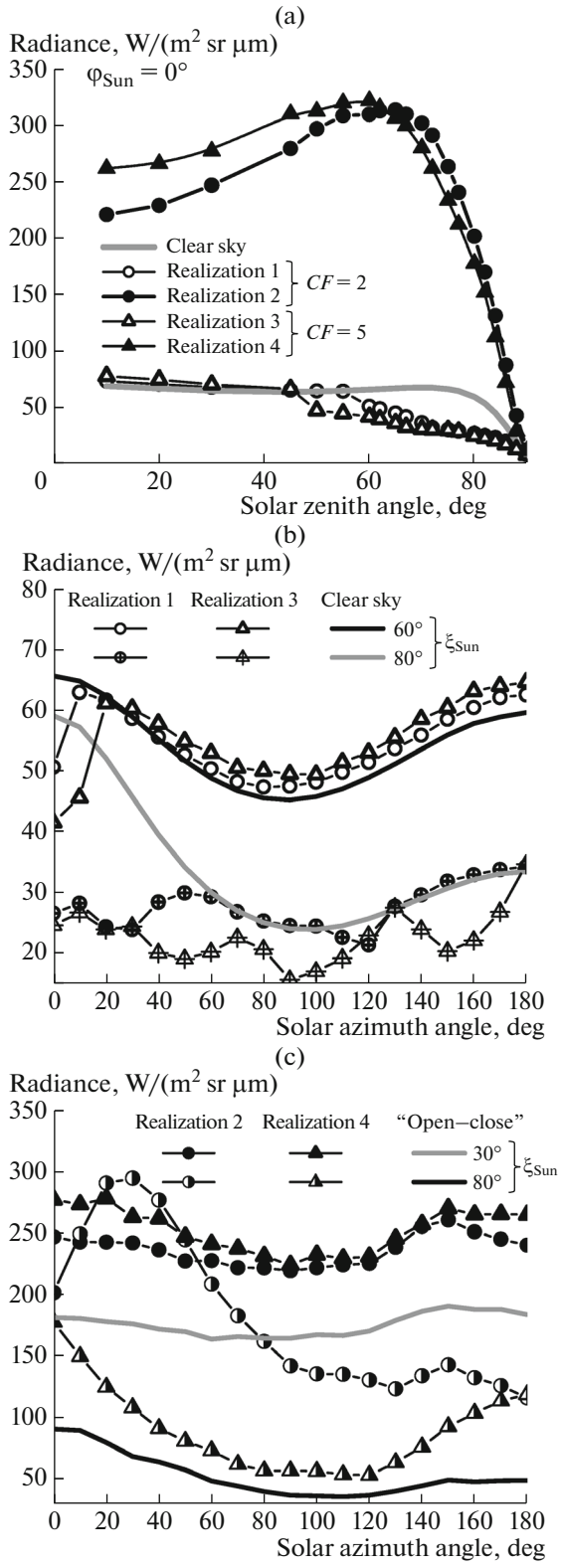

Fig. 4. Dependence of sky radiance in different cloud realizations on (a) zenith and (b, c) azimuth solar angles. Calculations in the "open–close" approximation are performed for the cloud fraction $CF = 5$ (c).

indicated calculation parameters, the cloud A does not shade the LS and OP, so that $I_{clr} \approx I_{cld}$. In the angular range of $55° < \xi_{Sun} < 82°$, the LS segment and LS are shaded, and the sky radiance is less than under clear-sky conditions. The inequality $I_{clr} \le I_{cld}$ remains valid as ξ_{Sun} further increases, when the OP becomes unobscured to direct solar rays, although the LS is still partially shaded. (This case is described in section 2: the case with $\varphi_{Sun} = 0$, cloud center is between points P_2 and P_3.) An analogous situation is also observed in realization 3. Since the cloud D, which shades LS, is closer to the point A' ($R_{cld} \approx 8.6$ km), the shading effect becomes apparent as early as $\xi_{Sun} > 45°$ (Fig. 4a).

The dependence of I_{cld} on the solar azimuth angle for both cloud realizations is presented in Fig. 4b. First, we note that, independent of cloud fraction, at $\xi_{Sun} = 60°$ the sky radiance in the presence of clouds is less than clear-sky radiance only in the above-mentioned narrow range of $\varphi_{Sun} < 10°$. As φ_{Sun} further increases, the broken-cloud radiance could change due to partial shading of LS by clouds lying in the direction "toward the Sun". However, in the realizations considered here, the shading effect is suppressed by additional illumination in the LS by cloud-reflected radiation, and in the region of $\varphi_{Sun} > 50°$ the radiance I_{cld} increases over clear-sky radiance.

The dependence of sky radiance on cloud configuration and amount is more significantly manifested as the solar zenith angle increases ($\xi_{Sun} = 80°$). Even though the LS is free of clouds, the inequality $I_{cld} \le I_{clr}$ holds in almost the entire range of solar azimuth angles for both realizations. This decrease in the sky radiance is explained by an enhancement of effects of LS shading (which is manifested for small cloud fractions, realization 1) and mutual cloud shading (which increases with the growing cloud fraction, realization 3). The sky radiance in the cloud field is close to clear-sky radiance (and even may exceed the latter due to illumination by nearby clouds) only for those directions of direct solar rays the propagation path of which is free of clouds. For instance, in realization 1, $I_{cld} \approx I_{clr}$ in the ranges $60° < \xi_{Sun} < 100°$ and $130° < \xi_{Sun} < 180°$; however, $I_{cld} < I_{clr}$ at $\varphi_{Sun} \approx 120°$. The probability that the LS and OP are shaded by clouds increases with the cloud fraction. From Fig. 3c it follows that, in realization 3, only within narrow zone near $\varphi_{Sun} \approx 130°$ and $\varphi_{Sun} \approx 180°$ the clouds are so far from OP that their presence does not lead to a change in sky radiance relative to the clear-sky radiance. For all other φ_{Sun} values, the inequality $I_{cld} < I_{clr}$ holds.

We will now consider realizations 2 and 4. In these, the sky radiance is determined by the presence of clouds B and E on the LS. The LS transects the cloud tops, which potentially ensures radiance "burst" due to appearance of additional scatterers in the form of cloud droplets and due to relatively minor attenuation

of radiation on the path from entry into the cloud to the LS segment on the sunlit side.

The dependence of sky radiance on solar zenith angle will be discussed by the example of case with $\varphi_{Sun} = 0$ (Fig. 4a).

In realization 2, the cloud *C*, in view of its proximity to the observation point, ensures additional illumination of LS and cloud *B*. At the same time, this cloud partially shades the LS and obscures the access of direct solar rays to OP up to $\xi_{Sun} \sim 80°$ (at $\xi_{Sun} > 80°$ OP becomes unobscured to unscattered radiation). However, the simulation results suggest that shading effect does not affect significantly the variations in sky radiance in appearance of other clouds, so that $I_{cld} \geq I_{clr}$ for all ξ_{Sun}.

Comparison of realizations shows that, in contrast to the cloud *B* (realization 2), the cloud *E* (realization 4) is surrounded by a densely populated circle of clouds. A consequence of this is enhanced effect of two opposite factors: on the one hand, re-reflected radiation between cloud elements and illumination of LS by element-reflected radiation; and, on the other hand, mutual shading of clouds and the LS. For $\xi_{Sun} < 60°–65°$, the radiance in realization 4 exceeds the radiance in realization 2, with this relationship remaining valid for all solar azimuth angles (Fig. 4c). Possibly, this radiance relationship is due to a stronger manifestation of cloud radiation interaction in passing from the low-cloud situation ($CF = 2$) to a realization with a moderate cloud fraction ($CF = 5$).

As the solar zenith angle further increases, the relationship between radiances changes (Figs. 4a and 4c), and radiance in realization 2 becomes larger than in realization 4. These results confirm the dominating role of shading effects for large oblique angles ξ_{Sun}. We also note that, when the solar azimuth angle varies, the sky radiance depends more strongly on the cloud configuration in the low-cloud situation than in the realization with a moderate cloud fraction (see sky radiances at $\xi_{Sun} = 80°$ in Fig. 4d).

Figure 4c presents values of outgoing TOA radiation calculated using the "open–close" approximation:

$$I_{cld}^{o-c} = (1 - 0.1CF)I_{clr} + 0.1\ CF\ I_{cld}^{(CF=10)}, \qquad (2)$$

where $I_{cld}^{(CF=10)}$ is the outgoing radiance in the presence of an overcast horizontally homogeneous cloud layer. The "open–close" approximation performs well when used to treat stratiform clouds, the horizontal extent of which substantially exceed their vertical sizes (the aspect ratio $\gamma = H_{cld}/2R_x \ll 1$); however, its use to describe the radiation characteristics in clouds with $\gamma \sim 1$ may lead to serious errors (see, e.g., [19]). Simulations show that approximation (2), used for the calculation in individual cloud realizations, may lead to either substantial underestimation or overestimation of sky radiance relative to values, calculated taking into account 3D cloud effects (I_{cld}^{3D}). For instance, at $\xi_{Sun} = 80°$ and $CF = 5$, for realization 4 the inequality $I_{cld}^{3D} \geq I_{cld}^{o-c}$ holds; whereas in realization 3 the reverse is true, $I_{cld}^{3D} < I_{cld}^{o-c}$.

CONCLUSIONS

The numerical simulation revealed the basic patterns of spatial-angular characteristics of sky radiance in the presence of isolated cloud and fields of clouds of vertical development in observations from space. The spherical model of the atmosphere makes it possible to estimate the effect of the spatial inhomogeneity of the deterministic cloud realization on the radiation characteristics of the atmosphere for large viewing and solar zenith angles (larger than 80°).

With the appearance of an isolated cloud in the sky, the sky radiance is determined by the cloud presence/absence on the LS, shading the LS by clouds/nonobscuration of direction "toward the Sun", as well as by illumination of the LS by cloud-reflected radiation. If the LS transects the cloud, the sky radiance may substantially exceed the clear-sky radiance, especially if the point of LS entry into the cloud is sunlit. Sky radiance decreases due to the effects of cloud shading of the LS and OP on the Earth's surface. The cloud impact zone may exceed several-fold the horizontal cloud sizes and substantially increases with solar and detector zenith angles.

The cloud fields were imitated using the model of Poisson point fluxes in space, uniformly distributed on the surface of a sphere. We considered four different cloud realizations for small and moderate cloud fractions. Considering the random character of the distribution of cloud elements (characteristic for the real atmosphere), the radiance for the specified illumination and observation conditions changes from one realization to another and, depending on the cloud configuration, may be either higher or lower than the clear-sky radiance. In the cloud fields, in addition to the above-mentioned 3D effects of isolated cloud, there are also the effects of radiation interaction, i.e., mutual shading and the effects of multiple scattering between the clouds. The results, presented in this paper, show that the specific features of broken cloud radiance field are mainly determined by cloud localization relative to two directions, i.e., the LS and direction "toward the Sun". In this sense, for certain sensing geometries, the difference in sky radiance between realizations with different cloud fractions may be less than the variability range of reflected radiation within the same realization. The effect of the cloud realization on angular characteristics of radiance field is more strongly manifested in slightly overcast situations because, as cloud amount grows, the uniform character of cloud distribution acts to smooth out the effects characteristic for isolated clouds.

ACKNOWLEDGMENTS

This work was supported in part by the Russian Foundation for Basic Research (grant no. 16-01-00617-a) and by the Ministry of Education and Science of the Russian Federation (T.V. Russkova, grant of the President of the Russian Federation no. MK-5381.2016.5).

REFERENCES

1. T. Varnai and A. Marshak, "Observations of three-dimensional radiative effects that influence modis cloud optical thickness retrievals," J. Atmos. Sci. **59** (9), 1607–1618 (2002).
2. H. Iwabuchi and T. Hayasaka, "A multi-spectral non-local method for retrieval of boundary layer cloud properties from optical remote sensing data," Remote Sens. Environ. **88** (3), 294–308 (2003).
3. A. Horvath and R. Davies, "Anisotropy of water cloud reflectance: A comparison of measurements and 1d theory," Geophys. Rev. Lett. **31** (1), L01102 (2004).
4. A. Marshak, S. Platnick, T. Varnai, G. Wen, and R. F. Cahalan, "Impact of 3D radiative effects on satellite retrievals of cloud droplet sizes," J. Geophys. Res., D **111** (9), DO9207 (2006).
5. E. I. Kassianov, M. Ovchinnikov, L. K. Berg, S. A. McFarlane, C. J. Flynn, R. Ferrare, C. Hostetler, and M. Alexandrov, "Retrieval of aerosol optical depth in vicinity of broken clouds from reflectance ratios: Case study," Atmos. Measur. Technol **3**, 1333–1349 (2010).
6. G. Wen, A. Marshak, R. Levy, L. Remer, N. Loeb, T. Varnai, and R. Cahalan, "Implementation of the correction algorithm of the MODIS aerosol retrievals near clouds," J. Geophys. Res., D **118** (16), 9168–9181 (2013).
7. A. Marshak, K. V. Evans, T. Varnai, and G. Wen, "Extending 3D near-cloud corrections from shorter to longer wavelengths," J. Quant. Spectrosc. Radiat. Transfer **147**, 79–85 (2014).
8. I. Koren, L. A. Remer, Y. J. Kaufman, Y. Rudich, and J. V. Martins, "On the twilight zone between clouds and aerosols," Geophys. Rev. Lett. **34** (8), L08805 (2007).
9. T. Varnai and A. Marshak, "MODIS observations of enhanced clear sky reflectance near clouds," Geophys. Rev. Lett. **36** (6), L06807 (2009).
10. J. C. Chiu, A. Marshak, Y. Knyazikhin, P. Pilewskie, and W. Wiscombe, "Physical interpretation of the spectral radiative signature in the transition zone between cloud-free and cloudy regions," Atmos. Chem. Phys. **9**, 1419–1430 (2009).
11. T. F. Eck, B. N. Holben, J. S. Reid, A. Arola, R. A. Ferrare, C. A. Hostetler, S. N. Crumeyrolle, T. A. Berkoff, E. J. Welton, S. Lolli, A. Lyapustin, Y. Wang, J. S. Schafer, D. M. Giles, B. E. Anderson, K. L. Thornhill, P. Minnis, K. E. Pickering, C. P. Loughner, A. Smirnov, and A. Sinyuk, "Observations of rapid aerosol optical depth enhancements in the vicinity of polluted cumulus clouds," Atmos. Chem. Phys. **14** (21), 11633–11656 (2014).
12. R. Z. Bar-Or, I. Koren, O. Altaratz, and E. Fredj, "Radiative properties of humidified aerosols in cloudy environment," Atmos. Res. **118**, 280–294 (2012).
13. G. Wen, A. Marshak, R. F. Cahalan, L. A. Remer, and R. G. Kleidman, "3D aerosol-cloud radiative interaction observed in collocated MODIS and ASTER images of cumulus cloud fields," J. Geophys. Res., D **112** (13), D13204 (2007).
14. G. Wen, A. Marshak, and R. F. Cahalan, "Impact of 3D clouds on clear sky reflectance and aerosol retrieval in a biomass burning region of Brazil," IEEE Geosci. Remote Sens. Lett. **3**, 169–172 (2006).
15. R. F. Cahalan, L. Oreopoulos, G. Wen, A. Marshak, S. C. Tsay, and T. P. DeFelice, "Cloud characterization and clear sky correction from Landsat-7," Remote Sens. Environ. **78**, 83–98 (2001).
16. T. Kobayashi, K. Masuda, M. Sasaki, and J. Mueller, "Monte Carlo simulations of enhanced visible radiance in clear-air satellite fields of view near clouds," J. Geophys. Res., D **105** (21), 26569–26576 (2000).
17. O. V. Nikolaeva, L. P. Bass, T. A. Germogenova, A. A. Kokhanovisky, V. S. Kuznetsov, and B. Mayer, "The influence of neighboring clouds on the clear sky reflectance with the 3D transport code RADUGA," J. Quant. Spectrosc. Radiat. Transfer **94**, 405–424 (2005).
18. M. A. Tarasenkov, I. V. Kirnos, and V. V. Belov, "Observation of the ground surface from space through a gap in the cloud field," Atmos. Ocean. Opt. **30** (1), 39–43 (2017).
19. V. E. Zuev and G. A. Titov, *Atmospheric Optics and Climate* (Spektr, Tomsk, 1996) [in Russian].
20. N. P. Kopytov and E. A. Mityushov, "Universal algorithm for uniform distribution of points over random analytical surfaces in 3D space," Fundam. Issled., No. 4–3, 618–622 (2013).
21. T. B. Zhuravleva, "Simulation of solar radiative transfer under different atmospheric conditions. Part I. The deterministic atmosphere," Atmos. Ocean. Opt. **21** (2), 81–97 (2008).
22. T. B. Zhuravleva, T. V. Bedareva, M. V. Kabanov, I. M. Nasrtdinov, and S. M. Sakerin, "Specific features of angular characteristics of diffuse solar radiation in a little-cloud atmosphere," Atmos. Ocean. Opt. **22** (6), 607–616 (2009).
23. G. I. Marchuk, G. A. Mikhailov, M. A. Nazaraliev, R. A. Darbinyan, B. A. Kargin, and B. S. Elepov, *Monte Carlo Method in Atmospheric Optics* (Nauka, Novosibirsk, 1976) [in Russia].
24. M. Hess, P. Koepke, and I. Schult, "Optical properties of aerosols and clouds: The software package OPAC," Bull. Amer. Meteorol. Soc. **79** (5), 831–844 (1998).
25. F. X. Kneizys, D. S. Robertson, L. W. Abreu, P. Acharya, G. P. Anderson, L. S. Rothman, J. H. Chetwynd, J. E. A. Selby, E. P. Shetle, W. O. Gallery, A. Berk, S. A. Clough, and L. S. Bernstein, *The MODTRAN 2/3 Report and LOWTRAN 7 Model* (Phillips Laboratory, Geophysics Directorate, Hanscom AFB, MA, 1996).
26. S. J. Hook, *ASTER Spectral Library: Johns Hopkins University (JHU) spectral library; Jet Propulsion Laboratory (JPL) spectral library; The United States Geological Survey (USGS-Reston) spectral library.* Dedicated CD-ROM. Version 1.2 (1998) (see also http://speclib.jpl.nasa.gov).

Translated by O. Bazhenov